Electronic Supplementary Information

Mechanism of poly(*N*-isopropylacrylamide) cononsolvency in aqueous methanol solutions explored *via* oxygen K-edge X-ray absorption spectroscopy

Masanari Nagasaka,*[ab] Fumitoshi Kumaki,[c] Yifeng Yao,[d] Jun-ichi Adachi [ce] and Kenji Mochizuki [d]

[a] *Institute for Molecular Science, Myodaiji, Okazaki 444-8585, Japan*
[b] *Molecular Science Program, Graduate Institute for Advanced Studies, SOKENDAI, Myodaiji, Okazaki 444-8585, Japan*
[c] *Photon Factory, Institute of Materials Structure Science, High Energy Accelerator Research Organization, 1-1 Oho, Tsukuba, Ibaraki 305-0801, Japan*
[d] *Department of Chemistry, Zhejiang University, Hangzhou, 310028, P. R. China*
[e] *Materials Structure Science Program, Graduate Institute for Advanced Studies, SOKENDAI, 1-1 Oho, Tsukuba, Ibaraki 305-0801, Japan*

*E-mail: nagasaka@ims.ac.jp

Table of Contents **Page**

Experimental and Theoretical Methods

Soft X-ray absorption spectroscopy

Soft X-ray absorption spectroscopy (XAS) experiments were performed at the soft X-ray beamline BL-7A of the Photon Factory, Institute of Materials Structure Science, High Energy Accelerator Research Organization (KEK-PF).[1] The energy resolution ΔE of soft X-rays was set to 0.29 eV at the O K-edge. The details of the transmission-type liquid cell for XAS have been described previously.[2, 3] The liquid cell was placed at ambient pressure conditions of helium gas, where a liquid layer was sandwiched between two Si_3N_4 membranes with a thickness of 100 nm. The thickness of the liquid layer was controlled by adjusting the helium pressure around the liquid cell. The beam size of soft X-rays was 200 × 200 μm^2 owing to the window size of the Si_3N_4 membrane, which separates the chamber of the liquid cell in the atmospheric helium condition and the soft X-ray beamline under an ultrahigh vacuum condition. The XAS spectra were obtained using the Beer-Lambert law, $\ln(I_0/I)$, where I_0 and I are the transmission signals of the bare Si_3N_4 membranes and liquid samples confined by the Si_3N_4 membranes, respectively. Liquid samples were exchanged using a syringe pump. The temperature of the liquid samples was controlled at 25 °C. The photon energies were calibrated precisely by measuring the XAS spectra of the polymer film before and after sample measurements.[4]

Poly(*N*-isopropylacrylamide) (PNIPAM) with Mn ~ 40,000 was purchased from Sigma-Aldrich. Methanol (MeOH) was purchased from FUJIFILM Wako Pure Chemical Co. Ultrapure water (H_2O) with a resistivity above 18 MΩ was used in our experiments. PNIPAM with a concentration of 50 mg/mL was dissolved in aqueous MeOH solutions $(MeOH)_x(H_2O)_{1-x}$ with different MeOH molar fractions. As shown in Sec. S2, PNIPAM is insoluble at $0.4 > x > 0.1$, a behavior known as cononsolvency.

Molecular Dynamics simulation

All-atom molecular dynamics (MD) simulations were performed using the GROMACS 2021.3 package.[5] The equation of motion was integrated using the Leapfrog algorithm with a time step of 2 fs. Under each condition, the initial conformation was first energy-minimized using a steep descent algorithm. A 2 ns equilibration was followed by a 1 μs production run at 300 K and 0.1 MPa, both under an isothermal-isobaric (*NpT*) ensemble. Temperature and pressure for production runs were controlled using a Nose-Hoover thermostat and Parrinello-Rahman barostat with dumpling constants being 0.5 ps and 1 ps, respectively, whereas Berendsen algorithm with a dumping constant of 2 ps was used for equilibration.

A single atactic (meso 47%) 40-mer PNIPAM chain was dissolved in 10,000 solvent molecules of MeOH and H_2O. A cubic simulation box was used to apply periodic boundary conditions in all directions. PNIPAM was represented by the OPLS-AA model.[6] The default partial charges were multiplied by a factor of 1.31, as proposed in previous studies.[7, 8] H_2O and MeOH molecules were represented by the SPC/E model[9] and KBFF model,[10] respectively. The nonbonded interactions were truncated at 1.4 nm without dispersion corrections. Long-range Coulombic interactions were evaluated using the particle-mesh Ewald algorithm. The Lennard-Jones parameters between different particles were determined using the Lorentz-Berthelot

combination rules:

$$\sigma_{ij} = \left(\sigma_{ii} + \sigma_{jj}\right)/2,\ \epsilon_{ij} = \sqrt{\epsilon_{ii}\epsilon_{jj}} \quad (1)$$

LINCS constraints are applied for all bonds.

Inner-shell calculation

Inner-shell calculations were conducted using the program package GSCF3.[11, 12] The ground and core excited states were calculated through the Hartree-Fock method, namely, ΔSCF (self-consistent field). The core-hole was frozen on a specified O atom in the SCF calculations for the core excited state. The relaxed Hartree-Fock potential for the O 1s ionized state was obtained by a partial SCF calculation within the orbital manifold orthogonalized to the valence excited state, whereas the Rydberg excited states were obtained using the improved virtual orbital method[13] to avoid spurious mixing between the valence and Rydberg orbitals. The present calculations do not include the zero-point vibrational energy. The scalar relativistic effect was not considered in the present calculation. The contracted Gaussian-type functions by Huzinaga et al. were used as primitive basis functions: (73/7) for C, N, and O, and (6) for H.[14] The contraction schemes were (3111121/3112/1*) for C, N, and O, and (42) for H atoms. The d-type polarization functions were used at the C atoms (ζ_d = 0.600), N atoms (ζ_d = 0.864), and O atoms (ζ_d = 1.154).

The structural optimizations of *N*-isopropylacrylamide (NIPAM) and PNIPAM, which consists of five polymer units of NIPAM, were performed using Gaussian 16.[15] The structural optimization was performed with B3LYP/aug-cc-pVDZ, considering the previous result for the formamide-H_2O complex.[16] The structures of MeOH and H_2O were also optimized with B3LYP/aug-cc-pVDZ. The hydrogen bond (HB) models of NIPAM and PNIPAM with MeOH and H_2O were determined from the results of the two-dimensional (2D) radial distribution function (RDF) obtained by MD simulations, as shown in Sec. S6.

Results and Discussion

S1. Detection Limit of PNIPAM in XAS Spectra

In the 50 mg/mL PNIPAM solutions, the concentration of the polymer unit is about 440 mM. The detection limit of the C=O π* peaks (532 eV) in the O K-edge XAS is 100 mM for separating the contribution of solvent MeOH and H_2O, whose first peaks are around 535 eV. Note that metal oxides have peaks below 530 eV.[17] In this case, the detection limit of the metal oxide peaks becomes lower and closer to 10 mM because the metal oxide peaks are far away from the absorbance of solvent MeOH and H_2O. The detection limit of C and N K-edge XAS in solvent H_2O is also low and close to 10 mM because these energy regions are well known as the water window.[18] In the solvent MeOH, on the other hand, it is difficult to measure C K-edge XAS spectra of solute molecules because the first peak of MeOH at the C K-edge is around 288 eV.[19] The C=C π* peaks (285 eV) such as benzene[20] and the C=N π* peaks (286 eV) such as pyridine[21] can be observed in the solvent MeOH because these peaks are below the first peak of MeOH. Because the energetic position of the C=O π* peaks are around 290 eV, the C=O π* peaks cannot be observed in the solvent MeOH. Therefore, PNIPAM in solvent MeOH only shows the C=O π* peaks in the O K-edge XAS, whose detection limit is above 100 mM. The detection limit of N K-edge XAS also becomes higher in the solvent MeOH. Soft X-rays at the N K-edge (400 eV) are also absorbed by solvent MeOH because the photon energy of the N K-edge is close to that of the C K-edge. In the soft X-ray beamline, monochromatic soft X-rays include not only first-order X-rays (400 eV) but also the high-order X-rays (800 eV, 1200 eV, *etc.*) due to the high order diffraction of a plane grating monochromator. Because of the absorption of the first-order X-rays (400 eV) by the solvent MeOH, the ratio of the high-order X-rays is increased compared to the first-order X-rays, resulting the increase of the detection limit of the N K-edge XAS.

As shown in Sec. S2, PNIPAM in aqueous MeOH solutions $(MeOH)_x(H_2O)_{1-x}$ at $0.4 > x > 0.1$ becomes a cloud solution because PNIPAM is insoluble in these aqueous MeOH solutions. In these cases, PNIPAM aggregates are floating in aqueous MeOH solutions. For exploring the measurement conditions of the O K-edge XAS of PNIPAM in aqueous MeOH solutions, the thickness of the samples for 1% transmission of soft X-rays at different photon energy was calculated from the previous theoretical results,[22] as shown in Fig. S1. In the calculations, the density of liquid H_2O was 1.0 g/cm^3, that of liquid MeOH was 0.792 g/cm^3, and that of solid PNIPAM was 1.386 g/cm^3. The thickness of liquid H_2O for 1% transmission of soft X-rays was 47.4 μm before the absorbance of H_2O and was 2.6 μm after the absorbance of H_2O at the O K-edge. The O K-edge XAS measurement of liquid H_2O needs the liquid layer below 1 μm. In the energy region of the C=O π* peaks of PNIPAM, on the other hand, soft X-ray can transmit the liquid layer with the thickness of 40 μm. The thick liquid layer should be prepared for the increase of the absorbance of the C=O π* peaks of PNIPAM. The thickness of liquid MeOH for 1% transmission of soft X-rays was 12.1 μm before the absorbance of MeOH and was 4.1 μm after the absorbance of MeOH at the O K-edge. As a result, the thickness of aqueous MeOH solution at $0.4 > x > 0.1$ would be between 10–40 μm for the transmission of soft X-rays in the energy region of the C=O π* peaks of PNIPAM. The thickness of solid PNIPAM for 1%

transmission of soft X-rays was 3.5 μm in the energy region of the C=O π* peaks of PNIPAM. It means that soft X-rays cannot transmit PNIPAM aggregates when the sizes of the aggregates are above several μm. The C=O π* peaks of PNIPAM are not observed when the concentrations of PNIPAM are below the detection limit (100 mM). Because the C=O π* peaks of PNIPAM were not observed at $0.4 > x > 0.1$ in the O K-edge XAS spectra of PNIPAM in aqueous MeOH solutions, the concentration of PNIPAM were below the detection limit and the sizes of the PNIPAM aggregates were above several μm in the aqueous MeOH solutions with the liquid thickness between 10–40 μm.

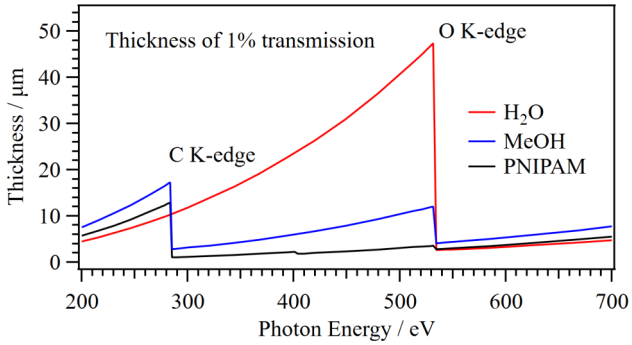

Figure S1. Thickness of liquid H_2O, liquid MeOH, and solid PNIPAM for 1% transmission of soft X-rays as a function of photon energy calculated from the previous theoretical results.[22]

S2. Photos of PNIPAM in Aqueous MeOH Solutions

Figure S2 shows photos of PNIPAM in aqueous MeOH solutions at different molar fractions. The solvent in the left bottle is pure H_2O ($x = 0.0$) and that in the right bottle is pure MeOH ($x = 1.0$). PNIPAM is completely dissolved with the solvents in both the MeOH-rich region ($x > 0.4$) and the H_2O-rich region ($0.1 > x$). PNIPAM is insoluble at $0.4 > x > 0.1$ and becomes a cloud solution. The deposition of PNIPAM is stronger by increasing the H_2O molar fraction and becomes a maximum value at $x = 0.1$.

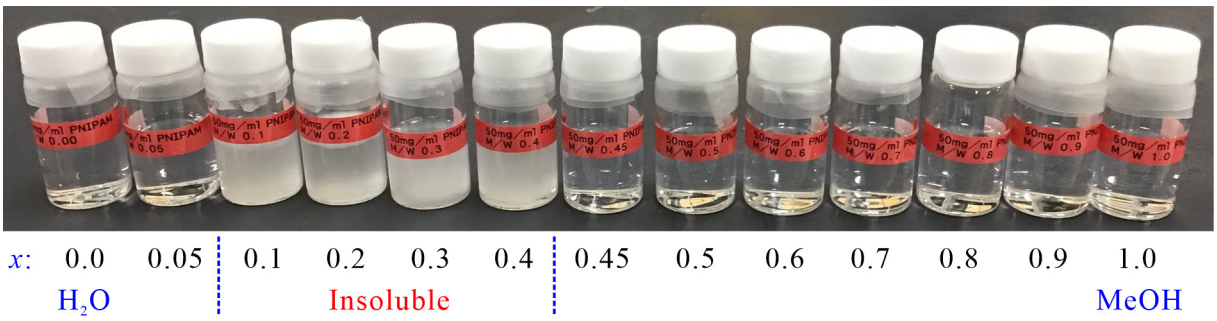

Figure S2. Photos of PNIPAM in aqueous MeOH solutions $(MeOH)_x(H_2O)_{1-x}$ at different molar fractions at a room temperature. PNIPAM is insoluble in the middle concentration region ($0.4 > x > 0.1$), a behavior known as cononsolvency.

S3. Time Evolution of Radius of Gyration

Figure S3 shows time evolution of radius of gyration (R_g) in aqueous MeOH solutions at different molar fractions (x = 0.0, 0.2, and 1.0). Note that pure H_2O (x = 0.0) and pure MeOH (x = 1.0) are good solvents for PNIPAM. We selected aqueous MeOH solution at x = 0.2, which represents the cononsolvency region ($0.4 > x > 0.1$). Two independent trajectories were shown at each concentration. The average values of R_g at each trajectory were also shown. As averaging all the trajectories at each concentration, we found that R_g = 1.78 ± 0.19 at x = 0.0, R_g = 1.71 ± 0.17 at x = 0.2, and R_g = 1.99 ± 0.16 at x = 1.0, respectively. The largest value of R_g at x = 1.0 means that PNIPAM chains in pure MeOH spread due to the weak interactions between polymer units. The polymer units are close to each other due to the strong interactions at x = 0.0, resulting the decrease of R_g. The smallest value of R_g at x = 0.2 means that the polymer units are aggregated and the deposition of PNIPAM is occurred.

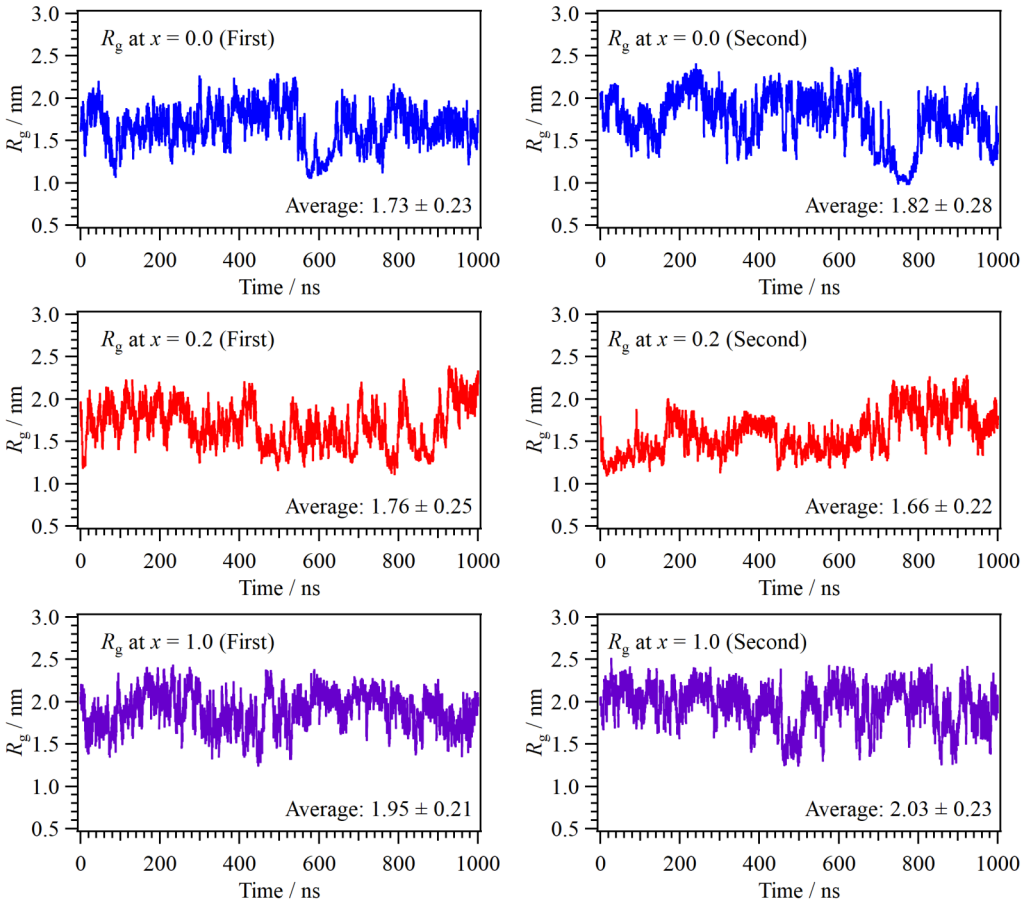

Figure S3. Time evolution of radius of gyration (R_g) of PNIPAM computed all atoms at x = 0.0, 0.2, and 1.0. Two independent trajectories at each x are shown. Note that R_g were calculated from all the trajectories at different MeOH molar fractions.

S4. Coordination Numbers of C=O Group in PNIPAM

Figure S4(a) shows RDF of oxygen atom (O_p) of the C=O group in PNIPAM with oxygen atom (O_w) of H_2O at x = 0.0 (H_2O) and x = 0.2. The position of the first coordination peak is 2.7 Å at x = 0.0, indicating the HB structures of the C=O group in PNIPAM with H_2O. Since the position of the first coordination peak is not nearly changed at x = 0.2, the HB structure of PNIPAM with H_2O at x = 0.2 is nearly same as that at x = 0.0. Figure S4(b) shows RDF of O_p with oxygen atom (O_m) of MeOH at x = 1.0 (MeOH) and x = 0.2. The position of the first coordination peak is 2.8 Å at x = 1.0, indicating the HB structure of C=O group in PNIPAM with MeOH. The longer distance of the first coordination peak (3.5 Å) in RDF of O_p with carbon atom (C_m) of MeOH also supports the HB structure of PNIPAM with MeOH. Since the position of the first coordination peak in RDF O_p – O_m at x = 0.2 is nearly close to that at x = 1.0, the HB structure of PNIPAM with MeOH at x = 0.2 is not changed compared to that at x = 1.0.

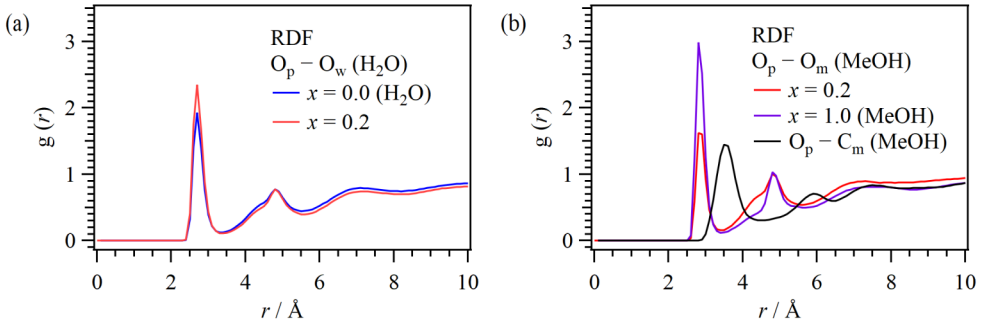

Figure S4. RDF of oxygen atom (O_p) of PNIPAM with oxygen atom (O_w) of H_2O and oxygen atom (O_m) of MeOH. (a) O_p – O_w in x = 0.0 (H_2O) and x = 0.2. (b) O_p – O_m in x = 0.2 and x = 1.0 (MeOH). RDF between O_p and carbon atom (C_m) of MeOH at x = 1.0 is also shown.

Table S1. Probability distributions of coordination numbers of O_p with O_w and O_m at x = 0.0, x = 0.2, and x = 1.0.

	0	1	2	3
O_p–O_w at x = 0.0	0.01	0.09	0.72	0.18
O_p–O_w at x = 0.2	0.04	0.34	0.55	0.07
O_p–O_m at x = 0.2	0.69	0.28	0.03	0.0
O_p–O_m at x = 1.0	0.05	0.58	0.36	0.01

From the first coordination peaks in RDF, we have determined the probability distributions of coordination numbers of MeOH and H_2O with the C=O group of PNIPAM, which are summarized in Table S1. In pure MeOH (x = 1.0), one or two MeOH molecules form HB structures with the C=O group of PNIPAM. The probability of one MeOH coordination is larger than that of two MeOH coordination. In the MeOH–H_2O

mixtures at x = 0.2, one or two H_2O molecules form HB structures with C=O group of PNIPAM, whereas zero or one MeOH molecules form the HB structures. By increasing the H_2O molar fraction from pure MeOH, total coordination numbers of MeOH and H_2O are close to two. The HB structure of H_2O with PNIPAM is easily formed compared to that of MeOH. In pure H_2O (x = 0.0), two H_2O molecules form HB structures with the C=O group of PNIPAM.

S5. Influences of Solvation Effects in Inner-Shell Calculations

Table S2 shows the photon energy of the C=O π* peaks in calculated O K-edge inner-shell spectra of NIPAM and PNIPAM with 5 polymer units including the solvent effects of MeOH or H_2O using the polarizable continuum model. The photon energy of the C=O π* peak of NIPAM including a solvent effect of MeOH was set to 0 meV. The C=O π* peak of NIPAM including a solvent effect of H_2O is −3 meV and is close to that including a solvent effect of MeOH. The C=O π* peak of NIPAM with no solvent effect shows a higher energy shift of 62 meV. Since the solvent effect of H_2O in NIPAM is close to that of MeOH, the inner-shell calculations of NIPAM were performed by using the molecular structure of NIPAM including the solvent effect of MeOH.

The C=O π* peak of PNIPAM including a solvent effect of H_2O shows the energy shift of −5 meV compared to that including a solvent effect of MeOH. On the other hand, the C=O π* peak of PNIPAM with no solvent effect shows a higher energy shift of 102 meV. Since the solvent effect of H_2O in PNIPAM is close to that of MeOH, the inner-shell calculations of PNIPAM were performed by using the molecular structures of PNIPAM with 5 polymer units including the solvent effect of MeOH.

Table S2. The photon energy of the C=O π* peaks in calculated O K-edge inner-shell spectra of NIPAM and PNIPAM including the solvent effects of MeOH or H_2O. The photon energy is relative to the C=O π* peak of NIPAM including a solvent effect of MeOH. The energy shifts (ΔE) of the C=O π* peaks in NIPAM and PNIPAM from same molecules including solvent effects of MeOH are also shown.

Molecule	Solvent	Energy / meV	ΔE / meV
NIPAM	–	62	62
	MeOH	0	0
	H_2O	−3	−3
PNIPAM	–	318	102
	MeOH	216	0
	H_2O	211	−5

S6. Two-Dimensional RDF around C=O Group in PNIPAM

For building the HB model structures of PNIPAM with MeOH and H_2O, we have calculated 2D RDF of O_p with O_m and O_w, as shown in Figure S5. Figure S5(a) shows 2D RDF $O_p - O_w$ in pure H_2O. The horizontal axes of both panels are the distance r between O_p and O_w. The vertical axis of the left panel is the angle θ between the normal vector of H_2O and r. The vertical axis of the right panel is the angle β between the C=O molecular axis of PNIPAM and r. From the left panel, we found that r = 2.7 Å and θ = 55°. We also found that β = 136° at r = 2.7 Å from the right panel. These results indicate that the HB structures of the C=O group in PNIPAM with H atom of H_2O is stable in pure H_2O. On the other hand, the peak around 5 Å is assigned as the HB structure between the NH group in PNIPAM with oxygen atom of H_2O.

Figure S5(b) shows 2D RDF $O_p - O_m$ in pure MeOH. The horizontal axes of both panels are the distance r between O_p and O_m. The vertical axis of the left panel is the angle θ between the O-CH_3 molecular axis of MeOH and r. The vertical axis of the right panel is the angle β between the C=O molecular axis of PNIPAM and r. From the left panel, we found that r = 2.8 Å and θ = 110°. We also found that β = 139° at r = 2.8 Å from the right panel. These results indicate that the HB structures of the C=O group in PNIPAM with H atom of MeOH is stable in pure MeOH. On the other hand, the peak around 5 Å is assigned as the HB structure between the NH group in PNIPAM with oxygen atom of MeOH.

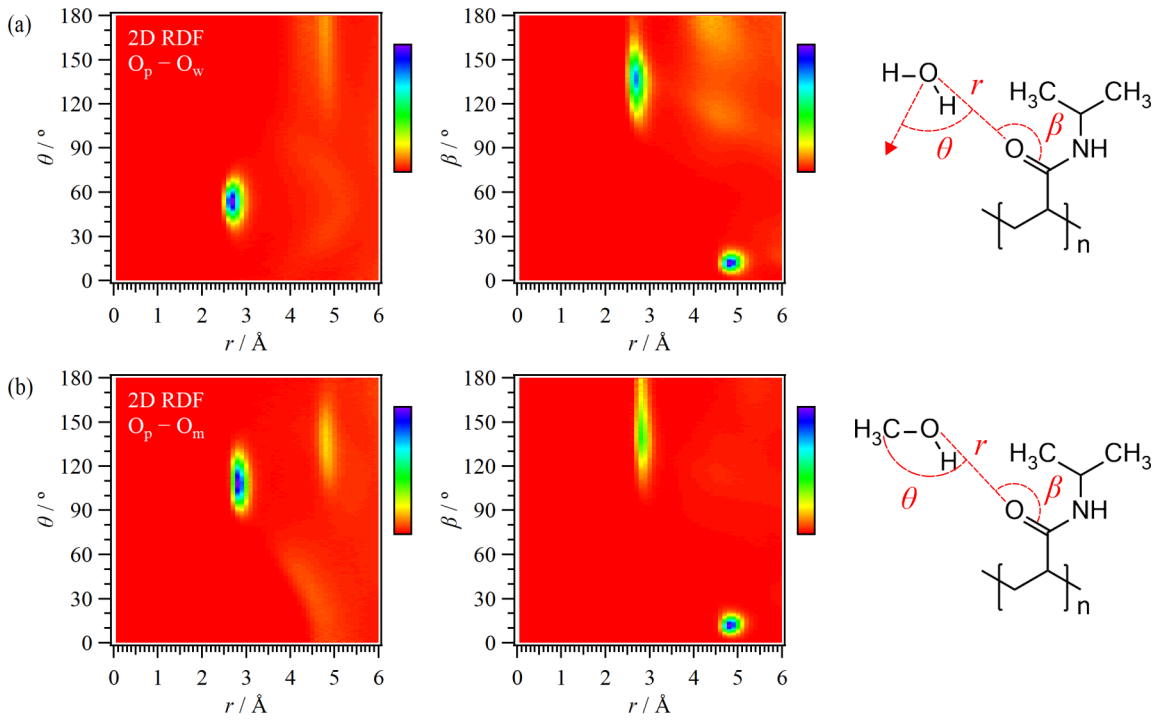

Figure S5. (a) 2D RDF $O_p - O_w$ in pure H_2O. The horizontal axes are the distance r between O_p and O_w. The vertical axes of the left and right panels are the angles θ and β, respectively, whose definitions are described in the inset. (b) 2D RDF $O_p - O_m$ in pure MeOH. The horizontal axes are the distance r between O_p and O_m. The vertical axes of the left and right panels are the angles θ and β, respectively, whose definitions are described in the inset.

S7. Inner-Shell Spectra of Different HB Structures of NIPAM and PNIPAM

Figure S6 shows inner-shell spectra of NIPAM with the HB structures of MeOH and H_2O. As discussed in Sec. S5, the molecular structure of NIPAM is optimized with including the solvent effect of MeOH. The HB structures of NIPAM with MeOH and H_2O were obtained from the distances and angles of the HB structures determined by 2D RDF described in Sec. S6. The C=O π* peak in the HB structure of NIPAM with one MeOH molecule shows a higher energy shift of 239 meV compared to that of isolated NIPAM molecule. The C=O π* peak in the HB structure of NIPAM with one H_2O molecule shows a higher energy shift of 276 meV. The C=O π* peaks in the HB structures of NIPAM with two MeOH, MeOH + H_2O, and two H_2O molecules are 457 meV, 460 meV, and 503 meV, respectively. Note that the energy shift of the C=O π* peak in the HB structures of NIPAM from MeOH + H_2O to two H_2O is 43 meV. The C=O π* peak shows a higher energy shift by increasing the coordination numbers of the HB structures of the C=O group in NIPAM with MeOH and H_2O. The C=O π* peak in the HB structure of NIPAM with H_2O shows a higher energy shift than that with MeOH.

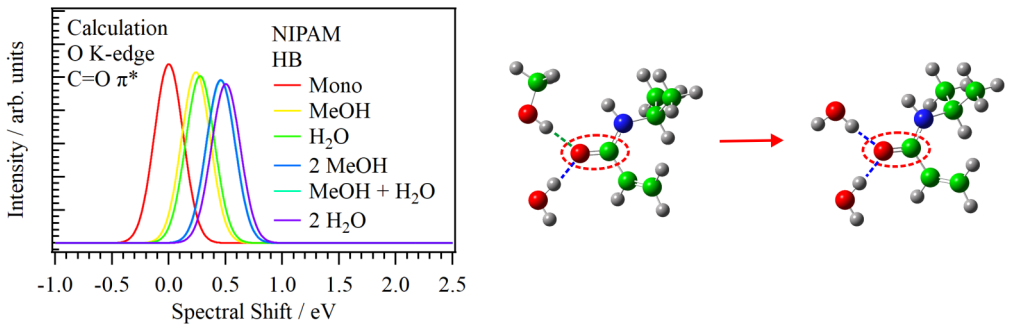

Figure S6. Calculated O K-edge inner-shell spectra of several HB structures of the C=O group in NIPAM with MeOH and H_2O molecules. The photon energy is relative to the C=O π* peak of an isolated NIPAM molecule. The inset shows HB structures of NIPAM with MeOH and H_2O molecules.

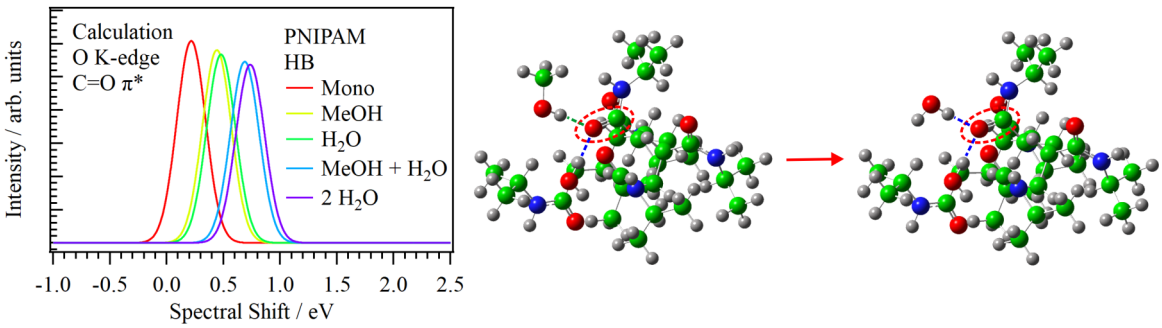

Figure S7. Calculated O K-edge inner-shell spectra of several HB structures of the C=O group in PNIPAM with H_2O and MeOH molecules. The photon energy is relative to the C=O π* peak of an isolated NIPAM molecule. The inset shows HB structures of PNIPAM with MeOH and H_2O molecules.

Figure S7 shows inner-shell spectra of PNIPAM with the HB structures of MeOH and H_2O. As discussed in Sec. S5, the molecular structure of PNIPAM with 5 polymer units was optimized with including the solvent effect of MeOH. The HB structures of PNIPAM with MeOH and H_2O were obtained from the distances and angles of the HB structures determined by 2D RDF described in Sec. S6. Note that the oxygen atom in the central polymer unit was only used in the inner-shell calculations of PNIPAM. The C=O π* peak of isolated PNIPAM polymer is 216 meV. The C=O π* peak in the HB structure of PNIPAM with one MeOH molecule is 442 meV. The C=O π* peak in the HB structure of PNIPAM with one H_2O molecule is 479 meV. The C=O π* peaks in the HB structures of PNIPAM with MeOH + H_2O and two H_2O molecules are 688 meV and 736 meV, respectively. Note that the energy shift of C=O π* peak in the HB structures of PNIPAM from MeOH + H_2O to two H_2O is 48 meV. Since the polymer units of PNIPAM were close to each other by the structural optimization, it is difficult to form the HB structures with two MeOH molecules. The PNIPAM chains spread in pure MeOH, and the C=O group in the polymer unit of PNIPAM can form the HB structures with two MeOH molecules in the actual environment. The C=O π* peak shows a higher energy shift by increasing the coordination numbers of the HB structures of the C=O group in PNIPAM with MeOH and H_2O. The C=O π* peak in the HB structure of PNIPAM with H_2O shows a higher energy shift than that with MeOH.

S8. Discussion of Structures of Aqueous MeOH Solutions

To elucidate the cononsolvency mechanism of PNIPAM, it is important to study the molecular interactions of MeOH and H_2O in aqueous MeOH solutions $(MeOH)_x(H_2O)_{1-x}$ with different molar fractions. Liquid MeOH (x = 1.0) has one- or two-dimensional HB chain structures, because MeOH has only one donor site.[23-28] On the contrary, liquid H_2O (x = 0.0) shows tetrahedrally coordinated three-dimensional HB network.[29] Mass[30] and Raman spectroscopies[31] revealed that the local structures of aqueous MeOH solutions show three concentration regions with borders at x = 0.7 and x = 0.3. This is because aqueous solutions are generally non-uniform and consist of microscopic cluster structures.[32] Using C K-edge XAS analysis, we also revealed that the hydrophobic interaction of the methyl group in MeOH exhibits three concentration regions with borders at x = 0.7 and x = 0.3.[19] In the MeOH-rich region (x > 0.7), the MeOH molecules formed chain structures with nearly zero influence from H_2O. The hydrophobic clusters of MeOH are formed at 0.7 > x > 0.3, which was also observed in the neutron scattering experiment.[33] In the H_2O-rich region (0.3 > x), the hydrophobic clusters are embedded in the three-dimensional HB network of H_2O owing to the decrease in the cluster size. The formed structures in aqueous MeOH solutions were also investigated using MD simulations.[34-36]

References

1 K. Amemiya, H. Kondoh, T. Yokoyama and T. Ohta, *J. Electron Spectrosc. Relat. Phenom.*, 2002, **124**, 151-164.

2 M. Nagasaka, H. Yuzawa and N. Kosugi, *Anal. Sci.*, 2020, **36**, 95-105.

3 M. Nagasaka and N. Kosugi, *Chem. Lett.*, 2021, **50**, 956-964.

4 M. Nagasaka, H. Yuzawa, T. Horigome and N. Kosugi, *J. Electron Spectrosc. Relat. Phenom.*, 2018, **224**, 93-99.

5 M. J. Abraham, T. Murtola, R. Schulz, S. Páll, J. C. Smith, B. Hess and E. Lindahl, *SoftwareX*, 2015, **1-2**, 19-25.

6 W. L. Jorgensen, J. D. Madura and C. J. Swenson, *J. Am. Chem. Soc.*, 1984, **106**, 6638-6646.

7 K. Mochizuki, T. Sumi and K. Koga, *Sci. Rep.*, 2016, **6**, 24657.

8 C. Dalgicdir and N. F. A. van der Vegt, *J. Phys. Chem. B*, 2019, **123**, 3875-3883.

9 H. J. C. Berendsen, J. R. Grigera and T. P. Straatsma, *J. Phys. Chem.*, 1987, **91**, 6269-6271.

10 S. Weerasinghe and P. E. Smith, *J. Phys. Chem. B*, 2005, **109**, 15080-15086.

11 N. Kosugi and H. Kuroda, *Chem. Phys. Lett.*, 1980, **74**, 490-493.

12 N. Kosugi, *Theor. Chim. Acta*, 1987, **72**, 149-173.

13 W. J. Hunt and W. A. Goddard, III, *Chem. Phys. Lett.*, 1969, **3**, 414-418.

14 S. Huzinaga, J. Andzelm, M. Klobukowski, E. Radzio-Andzelm, Y. Sakai and H. Tatewaki, *Gaussian Basis Sets for Molecular Calculations*, Elsevier, Amsterdam, 1984.

15 M. J. Frisch, G. W. Trucks, H. B. Schlegel, G. E. Scuseria, M. A. Robb, J. R. Cheeseman, G. Scalmani, V. Barone, G. A. Petersson, H. Nakatsuji, X. Li, M. Caricato, A. V. Marenich, J. Bloino, B. G. Janesko, R. Gomperts, B. Mennucci, H. P. Hratchian, J. V. Ortiz, A. F. Izmaylov, J. L. Sonnenberg, Williams, F. Ding, F. Lipparini, F. Egidi, J. Goings, B. Peng, A. Petrone, T. Henderson, D. Ranasinghe, V. G. Zakrzewski, J. Gao, N. Rega, G. Zheng, W. Liang, M. Hada, M. Ehara, K. Toyota, R. Fukuda, J. Hasegawa, M. Ishida, T. Nakajima, Y. Honda, O. Kitao, H. Nakai, T. Vreven, K. Throssell, J. A. Montgomery Jr., J. E. Peralta, F. Ogliaro, M. J. Bearpark, J. J. Heyd, E. N. Brothers, K. N. Kudin, V. N. Staroverov, T. A. Keith, R. Kobayashi, J. Normand, K. Raghavachari, A. P. Rendell, J. C. Burant, S. S. Iyengar, J. Tomasi, M. Cossi, J. M. Millam, M. Klene, C. Adamo, R. Cammi, J. W. Ochterski, R. L. Martin, K. Morokuma, O. Farkas, J. B. Foresman and D. J. Fox, Gaussian 16, Wallingford, CT, 2019.

16 M. Nagaraju and G. N. Sastry, *Int. J. Quant. Chem.*, 2010, **110**, 1994-2003.

17 M. Yoshida, Y. Mitsutomi, T. Mineo, M. Nagasaka, H. Yuzawa, N. Kosugi and H. Kondoh, *J. Phys. Chem. C*, 2015, **119**, 19279-19286.

18 T. W. Ford, A. D. Stead and R. A. Cotton, *Electron Microsc. Rev.*, 1991, **4**, 269-292.

19 M. Nagasaka, K. Mochizuki, V. Leloup and N. Kosugi, *J. Phys. Chem. B*, 2014, **118**, 4388-4396.

20 M. Nagasaka, H. Yuzawa, K. Mochizuki, E. Rühl and N. Kosugi, *J. Phys. Chem. Lett.*, 2018, **9**, 5827-5832.

21 M. Nagasaka, H. Yuzawa and N. Kosugi, *Z. Phys. Chem.*, 2018, **232**, 705-722.

22 C. T. Chantler, *J. Phys. Chem. Ref. Data*, 2000, **29**, 597-1048.

23 M. Magini, G. Paschina and G. Piccaluga, *J. Chem. Phys.*, 1982, **77**, 2051-2056.
24 A. H. Narten and A. Habenschuss, *J. Chem. Phys.*, 1984, **80**, 3387-3391.
25 Y. Tanaka, N. Ohtomo and K. Arakawa, *Bull. Chem. Soc. Jpn.*, 1984, **57**, 644-647.
26 Y. Tanaka, N. Ohtomo and K. Arakawa, *Bull. Chem. Soc. Jpn.*, 1985, **58**, 270-276.
27 S. Sarkar and R. N. Joarder, *J. Chem. Phys.*, 1993, **99**, 2032-2039.
28 T. Yamaguchi, K. Hidaka and A. K. Soper, *Mol. Phys.*, 1999, **96**, 1159-1168.
29 R. Ludwig, *Angew. Chem. Int. Ed.*, 2001, **40**, 1808-1827.
30 T. Takamuku, T. Yamaguchi, M. Asato, M. Matsumoto and N. Nishi, *Z. Naturforsch. A*, 2000, **55**, 513-525.
31 S. Dixit, W. C. K. Poon and J. Crain, *J. Phys.: Condens. Matter*, 2000, **12**, L323-L328.
32 H. Tang, J. Cai, C.-Y. Zhu, G.-J. Chen, X.-H. Wang and C.-Y. Sun, *J. Mol. Liq.*, 2022, **367**, 120382.
33 S. Trabelsi, M. Tlili, H. Abdelmoulahi, S. Bouazizi, S. Nasr, M. A. González, M.-C. Bellissent-Funel and J. Darpentigny, *J. Mol. Liq.*, 2022, **349**, 118131.
34 A. Laaksonen, P. G. Kusalik and I. M. Svishchev, *J. Phys. Chem. A*, 1997, **101**, 5910-5918.
35 I. Bakó, T. Megyes, S. Bálint, T. Grósz and V. Chihaia, *Phys. Chem. Chem. Phys.*, 2008, **10**, 5004-5011.
36 S. T. Moin, T. S. Hofer, B. R. Randolf and B. M. Rode, *J. Comput. Chem.*, 2011, **32**, 886-892.